





## RESEARCH ARTICLE

[View Article Online](#)  
[View Journal](#) | [View Issue](#)

 Cite this: *Mater. Chem. Front.*,  
2021, 5, 5142

# Enhanced upconversion luminescence and optical thermometry in Er<sup>3+</sup>/Yb<sup>3+</sup> heavily doped ZrO<sub>2</sub> by stabilizing in the monoclinic phase†

 Kexiu Wang, <sup>ab</sup> Hao Wu, <sup>\*a</sup> Guo-Hui Pan, <sup>\*a</sup> Huajun Wu, <sup>a</sup>  
 Liangliang Zhang <sup>a</sup> and Jiahua Zhang <sup>\*ab</sup>

Er<sup>3+</sup> and Yb<sup>3+</sup> heavily doped monoclinic ZrO<sub>2</sub> (m-ZrO<sub>2</sub>) stabilized by Nb<sup>5+</sup> is prepared by solid-state reactions. The upconversion luminescence (UCL) of concentration optimized m-ZrO<sub>2</sub>:2%Er<sup>3+</sup>,9%Yb<sup>3+</sup> shows a yellow emission which is found to be 4 times stronger than the red UCL of the optimized cubic ZrO<sub>2</sub>:2%Er<sup>3+</sup>,14%Yb<sup>3+</sup>. It is revealed that monoclinic ZrO<sub>2</sub> has faster radiative transition rates of Er<sup>3+</sup> and Yb<sup>3+</sup> than cubic ZrO<sub>2</sub> because of the lower crystal symmetry in the monoclinic phase that enables higher 4f–5d mixing of rare earth ions. The enhanced radiative transition allows 9%Yb<sup>3+</sup> in the monoclinic phase to have a similar absorption of 980 nm excitation light to that of 14%Yb<sup>3+</sup> in the cubic phase, thus retaining the lower energy back transfer from Er<sup>3+</sup> in the green emitting state to Yb<sup>3+</sup> and lower concentration quenching of Yb<sup>3+</sup> in the monoclinic phase. The green and red dual-color optical thermometry behavior of m-ZrO<sub>2</sub> has been explored. A large detectable temperature range, at which the absolute sensitivity is high, is realized through adopting this complementary optical thermometer. Repeated thermal experiments prove the stability of the m-ZrO<sub>2</sub> as a temperature probe. Our results indicate that heavily doped m-ZrO<sub>2</sub> is an excellent host for efficient luminescence of rare earth ions.

 Received 23rd March 2021,  
 Accepted 11th May 2021

DOI: 10.1039/d1qm00440a

[rsc.li/frontiers-materials](http://rsc.li/frontiers-materials)

## 1. Introduction

The near infrared (NIR) to visible upconversion (UC) luminescence (UCL) phenomenon has potential applications in fluorescence imaging, displays, temperature sensing, and so on.<sup>1–6</sup> In particular, the Er<sup>3+</sup>–Yb<sup>3+</sup> combination, which is the most popular UC system, typically produces green and red UCL under excitation of a 980 nm NIR laser. Yb<sup>3+</sup> acts as a sensitizer responsible for absorbing the IR excitation energy and transferring the energy to Er<sup>3+</sup> to realize energy transfer upconversion (ETU).<sup>7,8</sup> To achieve efficient luminescence, host materials with low cut-off phonon energies are usually used for suppressing the multiphonon relaxation (MPR) process. Generally, fluorides are efficient luminescent phosphors due to their low phonon energies. However, poor physical and chemical stabilities restrict their application, especially in aerobic and high temperature environments.<sup>9</sup>

Zirconia has relatively low phonon energy in oxides and it shows great potential as an efficient and stable luminescent host.<sup>10–15</sup> ZrO<sub>2</sub> displays a well-known polymorphism with three

different crystalline structures: monoclinic (m-ZrO<sub>2</sub>), tetragonal (t-ZrO<sub>2</sub>) and cubic (c-ZrO<sub>2</sub>), of which m-ZrO<sub>2</sub> is the ambient thermodynamically stable phase.<sup>16</sup> Moreover, m-ZrO<sub>2</sub> has the lowest crystal symmetry of C<sub>2</sub> site symmetry in three phases. Accordingly, the highest 4f–4f radiative transition rate of trivalent rare earth ions is expected in m-ZrO<sub>2</sub> among the three polymorphs because the low crystal symmetry is beneficial for the 4f–5d mixing.<sup>17–20</sup> The high radiative transition rate could enable enhanced absorption of excitation light, energy transfer (ET) rate and emission efficiency.

Liu and coworkers observed enhanced UCL in 0.5%Er<sup>3+</sup> singly doped m-ZrO<sub>2</sub> nanocrystals compared with that in t-ZrO<sub>2</sub>.<sup>20</sup> This enhancement was explained as the increase of the optical transition rate in m-ZrO<sub>2</sub>. Generally, a high concentration of Yb<sup>3+</sup> (~20%) is needed to achieve intense UCL. However, preparing rare earth heavily doped m-ZrO<sub>2</sub> faces a difficulty that trivalent rare earth ion substitution for Zr<sup>4+</sup> produces oxygen vacancies, which tend to stabilize in tetragonal or cubic phases rather than the monoclinic phase.<sup>21,22</sup> Thus, the effect of the m-ZrO<sub>2</sub> crystal field on UC characteristics of the Er<sup>3+</sup>–Yb<sup>3+</sup> system still remains unclear. Some studies have reported methods to stabilize in the monoclinic phase by codoping with Nb<sup>5+</sup> as charge compensation.<sup>23–25</sup> Here, we test the feasibility of this project in an Er<sup>3+</sup>–Yb<sup>3+</sup> system.

In this paper, the concentration optimized m-ZrO<sub>2</sub>:2%Er<sup>3+</sup>, 9%Yb<sup>3+</sup> stabilized by 11%Nb<sup>5+</sup> and c-ZrO<sub>2</sub>:2%Er<sup>3+</sup>, 14%Yb<sup>3+</sup>

<sup>a</sup> State Key Laboratory of Luminescence and Applications, Changchun Institute of Optics, Fine Mechanics and Physics, Chinese Academy of Sciences, Changchun 130033, China. E-mail: wuhao@ciomp.ac.cn, guohui.pan@aliyun.com, zhangjh@ciomp.ac.cn

<sup>b</sup> Center of Materials Science and Optoelectronics Engineering, University of Chinese Academy of Sciences, Beijing 100049, China

† Electronic supplementary information (ESI) available. See DOI: 10.1039/d1qm00440a

were prepared by solid-state reactions for comparative study. The UCL in m-ZrO<sub>2</sub> was found to be 4 times stronger than that in c-ZrO<sub>2</sub> and the monoclinic sample shows yellow UCL with intensity comparable to green and red emissions, while the cubic sample shows red UCL with almost negligible green emission. The above experimental results are studied based on the observation of the enhanced radiative transition rate in m-ZrO<sub>2</sub> by means of UCL, photoluminescence (PL), diffuse reflection (DR) spectra and fluorescence decay patterns. It is revealed that the increased radiative transition rates of Er<sup>3+</sup> and Yb<sup>3+</sup> in m-ZrO<sub>2</sub> play a key role in UCL enhancement. Finally, the temperature dependent UCL spectra of the Er<sup>3+</sup>/Yb<sup>3+</sup> heavily doped m-ZrO<sub>2</sub> are also studied for thermal sensing applications.

## 2. Experimental

### 2.1 Materials and synthesis

The m-ZrO<sub>2</sub>:xEr<sup>3+</sup>,yYb<sup>3+</sup> samples have the formula Zr<sub>1-2x-2y</sub>Er<sub>x</sub>Yb<sub>y</sub>Nb<sub>x+y</sub>O<sub>2</sub> with Nb<sup>5+</sup> for charge compensation. The c-ZrO<sub>2</sub>:xEr<sup>3+</sup>,yYb<sup>3+</sup> samples have the chemical formula Zr<sub>1-x-y</sub>Er<sub>x</sub>Yb<sub>y</sub>O<sub>2-x/2-y/2</sub> without the addition of Nb<sup>5+</sup>. To conduct a comparative study on the optimized m-ZrO<sub>2</sub>:2%Er<sup>3+</sup>,9%Yb<sup>3+</sup>, the singly doped m-ZrO<sub>2</sub>:xLn<sup>3+</sup> (Ln = Er, Yb) is used with the chemical formula Zr<sub>1-0.22Ln<sub>x</sub>Lu<sub>0.11-x</sub>Nb<sub>0.11</sub></sub>O<sub>2</sub> by the addition of Lu to keep the total concentration of rare earth unchanged. Similarly, the singly doped c-ZrO<sub>2</sub>:xLn<sup>3+</sup> (Ln = Er, Yb) with the chemical formula Zr<sub>1-0.16Ln<sub>x</sub>Lu<sub>0.16-x</sub>O<sub>2-0.08</sub></sub> is used for comparison with the optimized c-ZrO<sub>2</sub>:2%Er<sup>3+</sup>,14%Yb<sup>3+</sup>. The high purity materials ZrO<sub>2</sub> (A.R.), Er<sub>2</sub>O<sub>3</sub> (99.999%), Yb<sub>2</sub>O<sub>3</sub> (99.999%), Nb<sub>2</sub>O<sub>5</sub> (99.9%) and Lu<sub>2</sub>O<sub>3</sub> (99.99%) were weighed precisely according to certain stoichiometric ratios. Then the mixture was added with appropriate amounts of alcohol, and ground with a ball mill for 8 hours. Subsequently, it was calcined in a muffle furnace under an air atmosphere for 4 hours at 1450 °C. After natural cooling to room temperature in the furnace, all

the prepared samples were reground in an agate mortar to obtain the final powder.

### 2.2 Characterization

X-ray power diffraction (XRD) was carried out on a Bruker D8 Focus diffractometer for confirming the crystalline structure, which is operated at 40 kV and 30 mA, in the range from 10° to 80° with Cu-Kα (*l* = 1.54056 Å) radiation. The morphology of ZrO<sub>2</sub> was characterized by using a Hitachi S-4800 scanning electron microscope (SEM). The chemical element analysis and mapping were inspected on the S-4800 SEM equipped with an energy dispersive X-ray spectroscopy system (EDS, JEOL JXA-840).

### 2.3 Spectroscopy measurements

Steady state photoluminescence (PL) and UCL spectra were recorded by using a FLS920 spectrometer (Edinburgh Instruments) with a power controllable CW 980 nm laser diode (LD) as an excitation source. Using a Triax550 spectrometer (Horiba) and an optical parametric oscillator (OPO) as the excitation source, the decay curves were recorded, and the signals were analyzed by using a Tektronix digital oscilloscope (TDS3052). The diffuse reflectance (DR) spectra were recorded by using a UV-vis-NIR spectrophotometer (Shimadzu UV-3600plus). The temperature dependent luminescence behavior was obtained by using the Linkam THMS-600 hot stage and monitored by using a Qepro high performance spectrometer (Ocean Optics). Raman spectra were acquired on an Infinity Raman spectrometer (Horiba) with a 488 nm laser excitation source. All the measurements were carried out at room temperature unless deliberately mentioned.

## 3. Results and discussion

### 3.1 Structural characterization

The XRD patterns of Er<sup>3+</sup> and Yb<sup>3+</sup> doubly doped m-ZrO<sub>2</sub>:2%Er<sup>3+</sup>, 9%Yb<sup>3+</sup> and c-ZrO<sub>2</sub>:2%Er<sup>3+</sup>,14%Yb<sup>3+</sup> samples are shown in Fig. 1a.

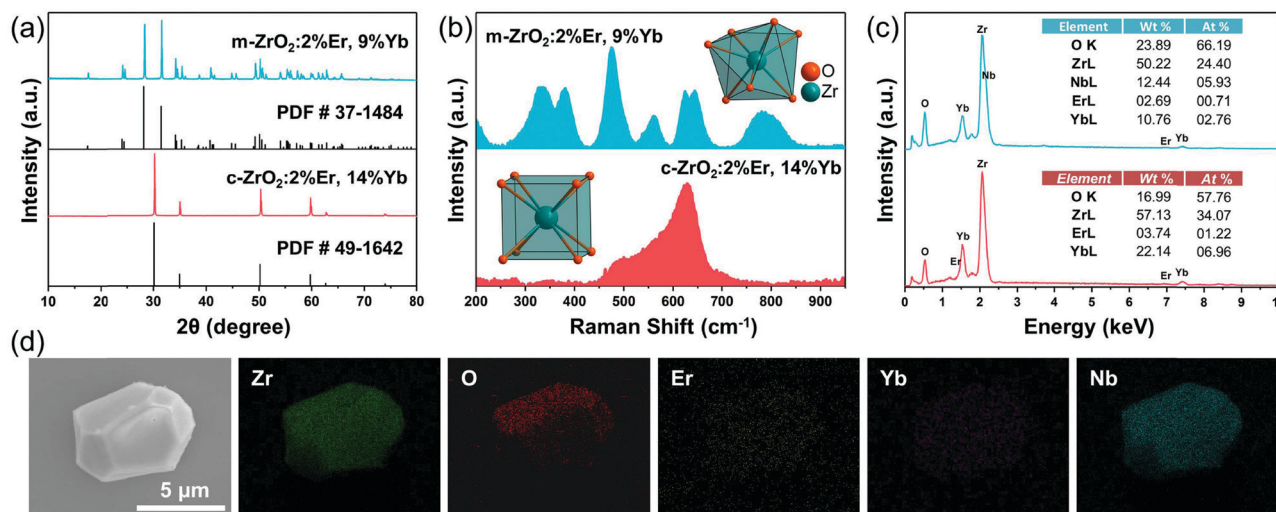


Fig. 1 (a) XRD patterns, (b) Raman spectra and (c) Raman spectra of concentration optimized m-ZrO<sub>2</sub> and c-ZrO<sub>2</sub>. The insets of (b) show the different site coordination structures in monoclinic and cubic phases. The insets of (c) show the approximate ratio of corresponding constituents. (d) The SEM image and elemental mappings of m-ZrO<sub>2</sub>:2%Er<sup>3+</sup>,9%Yb<sup>3+</sup>.

Both patterns show good consistence with the standard monoclinic pattern PDF#37-1484 and the cubic pattern PDF#49-1642, respectively. No obvious XRD peak of impurity phase is observed indicating that the doped rare earth and transition metal ions completely enter into the crystal lattices of  $\text{ZrO}_2$ . Raman spectroscopy is applied to additionally confirm the phase composition of two samples as presented in Fig. 1b. Six apparent Raman peaks at 330, 380, 476, 560, 624 and 645  $\text{cm}^{-1}$  are observed in the top panel of Fig. 1b, which are attributed to the vibration modes of the monoclinic phase.<sup>16,26,27</sup> Moreover, an extra peak at around 780  $\text{cm}^{-1}$  is caused by the Nb–O stretching vibration mode.<sup>26</sup> At the bottom of Fig. 1b, a single band at 630  $\text{cm}^{-1}$  is detected for the *c*- $\text{ZrO}_2$  sample, which is in accordance with the expected characteristic vibration of the cubic phase.<sup>27</sup> These results indicate that we have successfully prepared  $\text{Er}^{3+}$  and  $\text{Yb}^{3+}$  heavily doped pure phase *m*- $\text{ZrO}_2$  and *c*- $\text{ZrO}_2$  phosphors. In the insets of Fig. 1b, the *m*- $\text{ZrO}_2$  has only one crystallographic site ( $C_2$  symmetry) which is coordinated with seven oxygen atoms, while the *c*- $\text{ZrO}_2$  also possesses one cationic site ( $O_h$  symmetry) but the coordination number is eight. As a luminescent host lattice for trivalent rare earth ions, *m*- $\text{ZrO}_2$  is more attractive than *c*- $\text{ZrO}_2$  as a lower local symmetry could relax the parity selection rule.<sup>28,29</sup> From Fig. 1c it can be observed that the EDS spectra exhibit the major constituents and the corresponding atomic ratio in *m*- $\text{ZrO}_2$  and *c*- $\text{ZrO}_2$ , respectively. The detected atomic ratios are approximately equal to the designed stoichiometric ratios, even though it is not easy to obtain quantitative results accurately due to low dopant concentrations. The elemental mappings confirm the homogeneous distribution of all cationic elements in an individual *m*- $\text{ZrO}_2$  microcrystal, as shown in Fig. 1d.

### 3.2 Upconversion luminescence and kinetic analysis

The UCL spectra of the doping concentration optimized *m*- $\text{ZrO}_2$  and *c*- $\text{ZrO}_2$  are recorded under 980 nm LD excitation, as shown in Fig. 2a. The popular green emission around 550 nm and the red emission around 670 nm are observed in the spectra, which are derived from the  ${}^2\text{H}_{11/2} + {}^4\text{S}_{3/2} \rightarrow {}^4\text{I}_{15/2}$  and  ${}^4\text{F}_{9/2} \rightarrow {}^4\text{I}_{15/2}$  transitions of  $\text{Er}^{3+}$ , respectively. The UCL spectrum of the *m*- $\text{ZrO}_2$  shows both strong green and red emissions, but the red emission dominates the luminescence in the *c*- $\text{ZrO}_2$ . Moreover, the integrated intensity of UCL in the monoclinic sample is about 4 times stronger than that in the cubic sample. In general, the UCL intensity ( $I$ ) is dependent on the pump laser power ( $P$ ) according to the equation:  $I \propto P^n$ , where  $n$  is the number of absorbed photons in the UC process.<sup>30</sup> In the double logarithmic coordinate (see Fig. 2b), all the slopes are close to 2, mainly indicating the normal two-photon processes of the green and red UC emissions in both *m*- $\text{ZrO}_2$  and *c*- $\text{ZrO}_2$ .

In order to explore the reason for the UCL enhancement in *m*- $\text{ZrO}_2$ , the DR spectra of doubly doped *m*- $\text{ZrO}_2$ :2% $\text{Er}^{3+}$ , 9% $\text{Yb}^{3+}$  and *c*- $\text{ZrO}_2$ :2% $\text{Er}^{3+}$ , 14% $\text{Yb}^{3+}$  were recorded, as shown in Fig. 3a. It is clear that the two samples exhibit a similar  $\text{Yb}^{3+}$  absorbance around 980 nm although the  $\text{Yb}^{3+}$  concentration (9%) in the monoclinic sample is lower than that (14%) in the cubic sample. Meanwhile, the  $\text{Er}^{3+}$  absorption lines are

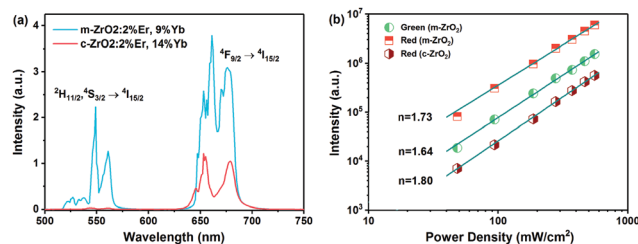


Fig. 2 UCL spectra of *m*- $\text{ZrO}_2$ :2% $\text{Er}^{3+}$ , 9% $\text{Yb}^{3+}$  and *c*- $\text{ZrO}_2$ :2% $\text{Er}^{3+}$ , 14% $\text{Yb}^{3+}$  under 980 nm excitation with the power density fixed at 500  $\text{mW cm}^{-2}$ . (b) Double logarithmic relationship of UC intensities versus laser power density in *m*- $\text{ZrO}_2$ :2% $\text{Er}^{3+}$ , 9% $\text{Yb}^{3+}$  and *c*- $\text{ZrO}_2$ :2% $\text{Er}^{3+}$ , 14% $\text{Yb}^{3+}$ .

markedly stronger in the monoclinic sample than those in the cubic sample in spite of the same  $\text{Er}^{3+}$  concentration of 2% for them. The DR spectra indicate that *m*- $\text{ZrO}_2$  significantly enhances the absorption cross-sections of doped rare earth ions compared with the cubic sample. The absorption enhancement is strongly supported by the observation of lifetime shortening of  ${}^2\text{F}_{5/2} \rightarrow {}^2\text{F}_{7/2}$  emission for 1% $\text{Yb}^{3+}$  singly doped or  ${}^4\text{I}_{13/2} \rightarrow {}^4\text{I}_{15/2}$  emission for 0.5% $\text{Er}^{3+}$  singly doped *m*- $\text{ZrO}_2$  in comparison with that of the cubic, as shown in Fig. 3b and c. Here, the lifetimes of the two emissions can be considered as the radiative lifetimes because the large energy gap ( $> 6500 \text{ cm}^{-1}$ ) and low doping concentrations ( $\leq 1\%$ ) substantially suppress the MPR and nonradiative decay through energy transfer. The measured lifetimes of the  $\text{Yb}^{3+} {}^2\text{F}_{5/2} \rightarrow {}^2\text{F}_{7/2}$  emission and  $\text{Er}^{3+} {}^4\text{I}_{13/2} \rightarrow {}^4\text{I}_{15/2}$  emission are 0.64 and 3.6 ms for the monoclinic as well as 1.86 and 9.1 ms for the cubic, exhibiting a 2.9-fold increase of the  ${}^2\text{F}_{5/2} \rightarrow {}^2\text{F}_{7/2}$  radiative rate and 2.5-fold increase of the  ${}^4\text{I}_{13/2} \rightarrow {}^4\text{I}_{15/2}$  radiative rate from the cubic to the monoclinic. The increase of the radiative rate that may be treated as absorption cross-sections is attributed to the increase of 4f–5d mixing driven by the low crystal symmetry of  $\text{Zr}^{4+}$  sites in the *m*- $\text{ZrO}_2$  structure.

The down-conversion emission spectra were also recorded while the UCL spectra were recorded upon 980 nm excitation, as shown in Fig. 3d. The spectra show the  $\text{Yb}^{3+} {}^2\text{F}_{5/2} \rightarrow {}^2\text{F}_{7/2}$  emission and  $\text{Er}^{3+} {}^4\text{I}_{13/2} \rightarrow {}^4\text{I}_{15/2}$  emission. One can see that *m*- $\text{ZrO}_2$  exhibits stronger infrared emissions than the cubic one. In view of the similar absorbance at 980 nm for the two samples, the stronger infrared emission in the monoclinic sample should have resulted from higher emission efficiencies. The efficient emission is attributed to the weak concentration quenching of the  $\text{Yb}^{3+}$  emission in *m*- $\text{ZrO}_2$  because of 9% $\text{Yb}^{3+}$  in the monoclinic phase being lower than 14% $\text{Yb}^{3+}$  in the cubic phase. Meanwhile, the increased absorption section in *m*- $\text{ZrO}_2$  can speed up the radiative rate and thus can enhance the emission. Based on the ETU mechanism in the  $\text{Er}^{3+}$ – $\text{Yb}^{3+}$  system, less concentration quenching of  $\text{Yb}^{3+}$  is beneficial for strong UCL because ETU for the green and red emissions requires two step energy transfer from  $\text{Yb}^{3+}$ . Moreover, high radiative rates in *m*- $\text{ZrO}_2$  enable efficient ETU and subsequent efficient emissions from the green and red emitting states in comparison with those in *c*- $\text{ZrO}_2$ .

To examine the efficacy of the green emission, the decay curves of the green emission were measured for the doubly



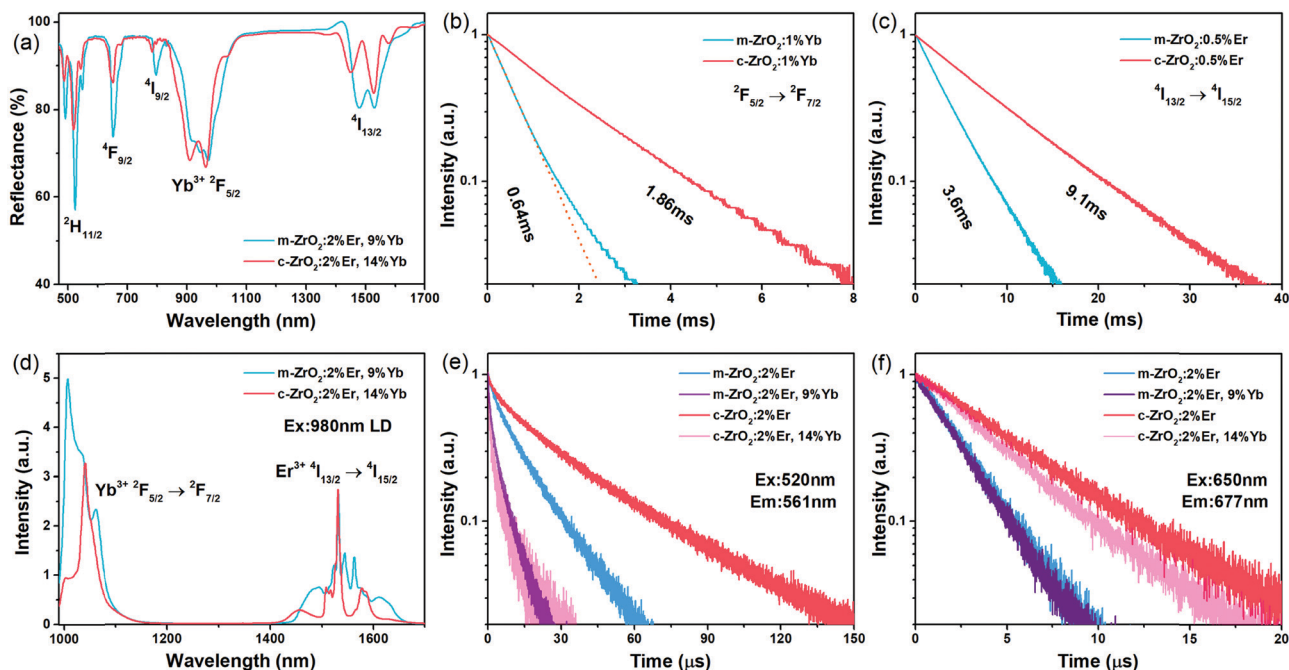


Fig. 3 (a) DR spectra of  $m\text{-ZrO}_2:2\%\text{Er}^{3+},9\%\text{Yb}^{3+}$  and  $c\text{-ZrO}_2:2\%\text{Er}^{3+},14\%\text{Yb}^{3+}$ . The fluorescence decay curves of (b)  $\text{Yb}^{3+} \ ^2\text{F}_{5/2}$  levels in  $m\text{-ZrO}_2:1\%\text{Yb}^{3+}$  and  $c\text{-ZrO}_2:1\%\text{Yb}^{3+}$  as well as (c)  $\text{Er}^{3+} \ ^4\text{I}_{13/2}$  levels in  $m\text{-ZrO}_2:0.5\%\text{Er}^{3+}$  and  $c\text{-ZrO}_2:0.5\%\text{Er}^{3+}$  upon direct excitation of the emitting levels. (d) The photoluminescence spectra of  $m\text{-ZrO}_2:2\%\text{Er}^{3+},9\%\text{Yb}^{3+}$  and  $c\text{-ZrO}_2:2\%\text{Er}^{3+},14\%\text{Yb}^{3+}$  under 980 nm laser excitation with the same power density as the UCL measurement. The fluorescence decay curves of (e) green and (f) red emissions for different samples.

doped and  $2\%\text{Er}^{3+}$  singly doped  $\text{ZrO}_2$ , as shown in Fig. 3e. One can observe a shortening of the emission lifetime from  $\text{Er}^{3+}$  singly doped to  $\text{Er}^{3+}$  and  $\text{Yb}^{3+}$  doubly doped  $\text{ZrO}_2$ . The lifetime shortening is well known to have been caused by cross relaxation (CR) from  $\text{Er}^{3+} \ ^4\text{S}_{3/2}$  down to  $\text{Er}^{3+} \ ^4\text{I}_{13/2}$  bypassing the intermediated levels through energy transfer to  $\text{Yb}^{3+}$ , as shown in Fig. 4a. The CR results in an excited  $\text{Er}^{3+}\text{-Yb}^{3+}$  pair with the  $\text{Er}^{3+}$  in the  $^4\text{I}_{13/2}$  excited state and  $\text{Yb}^{3+}$  in the  $^2\text{F}_{5/2}$  excited state. One can see that the lifetime reduction in  $c\text{-ZrO}_2$  is more apparent than that in  $m\text{-ZrO}_2$  due to the higher  $\text{Yb}^{3+}$  concentration in the cubic phase. The green lifetime in the doubly doped  $c\text{-ZrO}_2$  is shorter than that in the monoclinic sample, implying much lower green emission efficiency in the cubic

sample, because  $c\text{-ZrO}_2$  also has a lower radiative rate than  $m\text{-ZrO}_2$ . As a result, a very weak green UC emission is observed in  $c\text{-ZrO}_2:2\%\text{Er}^{3+},14\%\text{Yb}^{3+}$ . It should be noted that  $\text{Er}^{3+}$  singly doped  $m\text{-ZrO}_2$  has a shorter green emission lifetime than  $\text{Er}^{3+}$  singly doped  $c\text{-ZrO}_2$ . This behavior can be explained as stronger electron-phonon coupling and shorter radiative lifetime in  $m\text{-ZrO}_2$  than that in  $c\text{-ZrO}_2$  because of the lower crystal symmetry in  $m\text{-ZrO}_2$ . Similar behavior is also observed for the red emission lifetimes. The red lifetime in  $c\text{-ZrO}_2$  is about twice as that in  $m\text{-ZrO}_2$  for both  $\text{Er}^{3+}$  singly and doubly doped  $\text{ZrO}_2$  (see Fig. 3f). In view of that the radiative rate in  $m\text{-ZrO}_2$  is more than twice that in  $c\text{-ZrO}_2$ ,  $m\text{-ZrO}_2$  still has a higher red emission efficiency than  $c\text{-ZrO}_2$ . The red lifetime is insensitive to  $\text{Yb}^{3+}$

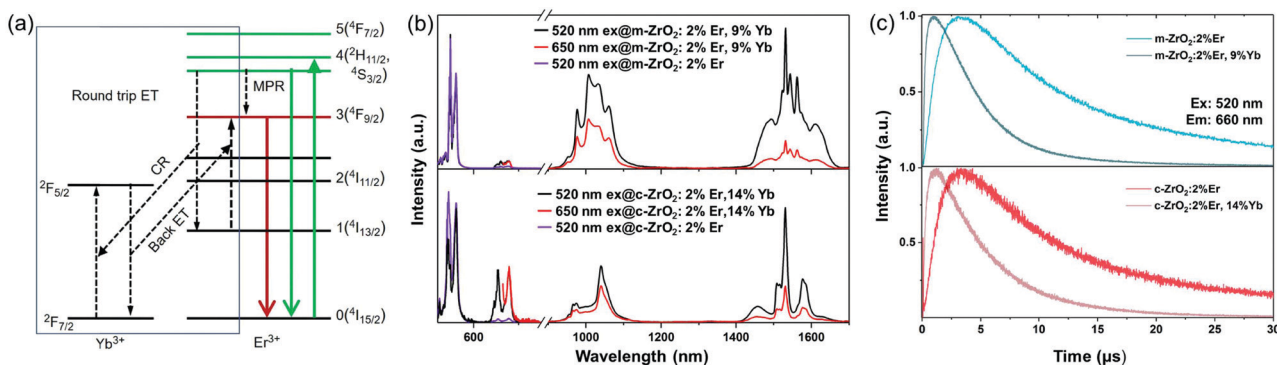


Fig. 4 (a) Schematic energy level diagram of the round trip energy transfer for red population in the  $\text{Er}^{3+}\text{-Yb}^{3+}$  system. (b) PL spectra of doubly doped samples under 520 and 650 nm excitation and the red emission intensities are normalized. PL spectra of singly doped samples upon 520 nm excitation and the green emission intensities are normalized to that of doubly doped samples. (c) Time evolutions of the red emission upon 520 nm excitation.

addition because of the absence of energy transfer from excited  $\text{Er}^{3+}$  in the red emitting state to  $\text{Yb}^{3+}$  in its ground state.<sup>7,31</sup>

### 3.3 Round trip energy transfer for red population from green state

The stronger red UC emission than the green emission is also contributed from a population process from the green  $^4\text{S}_{3/2}$  state to the red  $^4\text{F}_{9/2}$  state, proposed in our previous work.<sup>7</sup> This process is not MPR, but a round trip energy transfer between a  $\text{Er}^{3+}$ - $\text{Yb}^{3+}$  pair with CR as the forward step followed by the energy back transfer from  $\text{Yb}^{3+}$  to the original  $\text{Er}^{3+}$  in the  $^4\text{I}_{13/2}$  state to promote the red state population, as sketched in Fig. 4a. The PL spectra of the doubly doped samples are recorded upon  $^2\text{H}_{11/2}$  excitation at 520 nm or upon  $^4\text{F}_{9/2}$  excitation at 650 nm, as shown in Fig. 4b, wherein only 520 nm excitation can drive the round trip process. The PL spectra of  $\text{Er}^{3+}$  singly doped samples are also recorded upon 520 nm excitation for comparison with the doubly doped samples. One finds that the red emission in the doubly co-doped samples (black line) is stronger than that in  $\text{Er}^{3+}$  singly doped samples (purple line), indicating the importance of the round trip process. Particularly in doubly doped *c*- $\text{ZrO}_2$  the red emission is much stronger than that in  $\text{Er}^{3+}$  singly doped *c*- $\text{ZrO}_2$ , indicating the predominant round trip process rather than the traditional  $^4\text{S}_{3/2} \rightarrow ^4\text{F}_{9/2}$  MPR for  $^4\text{F}_{9/2}$  population from  $^4\text{S}_{3/2}$ . One may wonder if the enhanced red emission is due to the enhanced green to red MPR rather than the round trip process. To keep MPR unchanged after the addition of  $\text{Yb}^{3+}$ , the 2% $\text{Er}^{3+}$  singly doped samples are also doped with 9% or 14%  $\text{Lu}^{3+}$  for maintaining a constant content of rare earth ions, which possess similar vibronic frequencies and then should offer close MPR rates.

The CR produces excited  $\text{Yb}^{3+}$  in the  $^2\text{F}_{5/2}$  state and excited  $\text{Er}^{3+}$  in the  $^4\text{I}_{13/2}$  state. By comparing the spectra upon  $^2\text{H}_{11/2}$  excitation with that upon  $^4\text{F}_{9/2}$  excitation in the  $\text{Er}^{3+}/\text{Yb}^{3+}$  co-doped samples, one can observe that there is an extra intensity in both  $^2\text{F}_{5/2} \rightarrow ^2\text{F}_{7/2}$  and  $^4\text{I}_{13/2} \rightarrow ^4\text{I}_{15/2}$  emissions for  $^2\text{H}_{11/2}$  excitation, which obviously reflects the consequences of CR. The generated excited  $\text{Yb}^{3+}$ - $\text{Er}^{3+}$  pairs by CR may cooperate for the promotion of  $^4\text{F}_{9/2}$  population to complete round trip energy transfer or relax individually. The round trip process consumes the excited  $\text{Yb}^{3+}$ - $\text{Er}^{3+}$  pairs to produce red emission, therefore the extra  $\text{Yb}^{3+}$  or  $\text{Er}^{3+}$  emission intensity for  $^2\text{H}_{11/2}$  excitation is just the part that does not complete the round trip energy transfer. The generated red population by the round trip process mostly relaxes down to the  $^4\text{I}_{11/2}$  state, where it transfers energy to  $\text{Yb}^{3+}$  or continuously relaxes down to the  $^4\text{I}_{13/2}$  state. The population distribution among  $\text{Er}^{3+}$   $^4\text{F}_{9/2}$ ,  $^4\text{I}_{11/2}$ ,  $^4\text{I}_{13/2}$ , and  $\text{Yb}^{3+}$   $^2\text{F}_{5/2}$  populated from  $^4\text{F}_{9/2}$  can be known from the emission spectra upon  $^4\text{F}_{9/2}$  excitation (red in Fig. 4b). Based on the analysis above, the ratio of the  $\text{Yb}^{3+}$  emission intensity upon  $^4\text{F}_{9/2}$  excitation to that upon  $^2\text{H}_{11/2}$  excitation is the probability of the round trip process after CR. It is clear that the cubic sample has a higher probability of the round trip process than the monoclinic sample. From both UCL and PL spectra (Fig. 2a and 4b), one may note that the high red to green ratio in the cubic sample is in part contributed from the round trip process. The dynamical process of the round trip energy transfer is

studied based on the measurements of time evolutions of the red emission after the green state is excited, as shown in Fig. 4c. The temporal behavior of the red emission in  $\text{Er}^{3+}$  singly doped samples show a usual rising edge corresponding to the  $^4\text{F}_{9/2}$  state lifetime followed with a decay corresponding to the green  $^4\text{S}_{3/2}$  lifetime. Surprisingly, the red emission in  $\text{Er}^{3+}/\text{Yb}^{3+}$  doubly codoped samples shows a fast rising edge followed by a decay corresponding to the  $^4\text{F}_{9/2}$  state lifetime. Similar behavior was observed previously and it is attributed to fast round trip energy transfer between the nearest  $\text{Er}^{3+}$ - $\text{Yb}^{3+}$  pairs.<sup>7</sup> The fast population from the green to red state, therefore, leads to a decay with the red  $^4\text{F}_{9/2}$  state lifetime.

### 3.4 Optical thermometry behavior

It is well known that the  $\text{Er}^{3+}$   $^2\text{H}_{11/2}$  and  $^4\text{S}_{3/2}$  green energy levels are thermally coupled because of their appropriate energy gap ( $\sim 800 \text{ cm}^{-1}$ ). The fluorescence intensity ratio (FIR) of  $^2\text{H}_{11/2} \rightarrow ^4\text{I}_{15/2}$  emission to  $^4\text{S}_{3/2} \rightarrow ^4\text{I}_{15/2}$  emission is thus highly sensitive to temperature, exhibiting excellent behavior for temperature sensing.<sup>32,33</sup> Besides, some research studies have also reported that the red emission can be used for thermometry.<sup>11,34</sup> The *m*- $\text{ZrO}_2$ :2% $\text{Er}^{3+}$ ,9% $\text{Yb}^{3+}$  can not only produce strong red UC emissions, but also strong green UC emissions, showing attractive potential for temperature sensing based on the FIR technique. Herein, the UCL spectra of the green and red emissions for *m*- $\text{ZrO}_2$ :2% $\text{Er}^{3+}$ ,9% $\text{Yb}^{3+}$  were measured upon 980 nm LD excitation at different temperatures to verify its potential to be an optical thermometer. Under 980 nm LD excitation, it is observed that the FIR of  $^2\text{H}_{11/2}$ - $^4\text{I}_{15/2}$  emission to  $^4\text{S}_{3/2}$ - $^4\text{I}_{15/2}$  emission of  $\text{Er}^{3+}$  in the UCL spectra is almost the same as that in the PL spectra under 488 nm excitation of a xenon lamp at room temperature, indicating that the laser-induced thermal effect can be neglected.<sup>32</sup> As shown in Fig. 5a and Fig. S2 (ESI<sup>†</sup>), the green emissions are normalized to the 549 nm peak and the red ones are normalized to the 662 nm peak for conveniently observing the relative intensity variations as a function of temperature. Obviously, the  $^2\text{H}_{11/2} \rightarrow ^4\text{I}_{15/2}$  emission intensity monotonously grows up with the increase of temperature from 83 to 563 K without a clear change of peak positions but intensities. As for the red ones, it is easy to observe a homologous feature that the 654 nm peak boosts with the increase of temperature, implying the ability of the red scheme for temperature sensing. The excitation and emission spectra at liquid nitrogen temperature and room temperature were used for qualitatively explaining the principle of a red thermometer, as shown in Fig. S3 (ESI<sup>†</sup>). The  $^4\text{F}_{9/2}$  manifold will mostly populate its lowest Stark level at 77K and the strong emission peaks reflect the split of the  $^4\text{I}_{15/2}$  level. The appearance of the excitation band at 667–690 nm in the RT excitation spectrum confirms the thermally populated Stark levels of the ground state. Analogously, the  $^4\text{I}_{15/2}$  manifold mostly populates its lowest Stark level at 77 K and the strong excitation band reflects the split of the  $^4\text{F}_{9/2}$  level. At 77 K, it is easy to find the 654 and 662 nm peaks within the strong excitation band, indicating that these two peaks originate from different Stark levels of  $^4\text{F}_{9/2}$ . Consequently, the FIR of 654 nm to 662 nm peaks increases rapidly with the increase of temperature. Here, we do not select the 671, 675 and 680 nm peaks

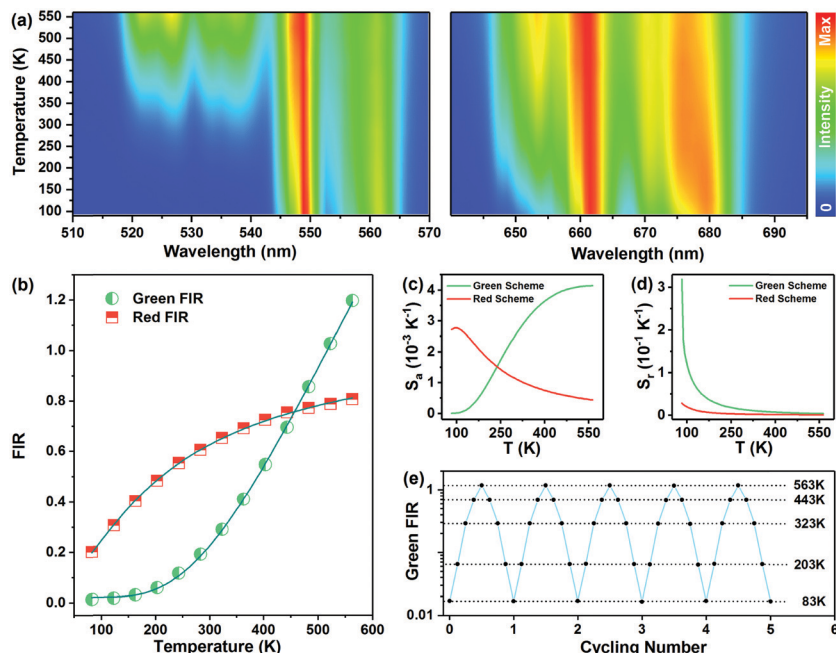


Fig. 5 (a) Temperature-dependent emission contour plots of the m-ZrO<sub>2</sub>:2%Er<sup>3+</sup>,9%Yb<sup>3+</sup> sample. The emission intensities at 549 and 662 nm are normalized, respectively. Dependence of (b) FIR, (c)  $S_a$  and (d)  $S_r$  versus the temperature of green and red emissions of the m-ZrO<sub>2</sub>:2%Er<sup>3+</sup>,9%Yb<sup>3+</sup>. (e) The single logarithm of green FIR plotted per cycle step. The dashed lines are the average values at the specific temperature.

due to their more terrible spectral overlap and complex peak division process. Following the Boltzmann distribution law for two thermally coupled levels, the FIR of the upper level to the lower level can be simply expressed as:<sup>35</sup>

$$\text{FIR} = B \exp\left(-\frac{\Delta E}{KT}\right) + C \quad (1)$$

where  $\Delta E$ ,  $K$ ,  $T$ ,  $B$  and  $C$  are the energy gap between the two levels, Boltzmann constant, absolute temperature, fitting constant and the offset, respectively. The temperature dependent FIRs of <sup>2</sup>H<sub>11/2</sub> to <sup>4</sup>S<sub>3/2</sub> and <sup>4</sup>F<sub>9/2(1)</sub> to <sup>4</sup>F<sub>9/2(0)</sub> (654 nm/662 nm) are obtained from Fig. 5b and they are well fitted using eqn (1) with  $B$  of 8.576 and 1.002 for green and red schemes, individually. Meanwhile, we can also obtain the  $\Delta E$  of 780 cm<sup>-1</sup> for the energy separation between the <sup>2</sup>H<sub>11/2</sub> and <sup>4</sup>S<sub>3/2</sub>, and 135 cm<sup>-1</sup> for that between Stark levels of the <sup>4</sup>F<sub>9/2</sub> level.

The absolute sensitivity ( $S_a$ ) and relative sensitivity ( $S_r$ ), as the vital parameters in practical applications, characterize the thermometric capability of materials. According to the definition of the sensitivities and using eqn (1), they can be calculated using the below equations:<sup>33,36</sup>

$$S_a = \frac{d\text{FIR}}{dT} = \text{FIR} \frac{\Delta E}{KT^2} \quad (2)$$

$$S_r = \frac{1}{\text{FIR}} \frac{d\text{FIR}}{dT} = \frac{\Delta E}{KT^2} \quad (3)$$

The calculated  $S_a$  and  $S_r$  as a function of temperature are plotted in Fig. 5c and d. It can be clearly observed that the  $S_r$  monotonically decreases with the increase of temperature. Diversely, the  $S_a$  keeps increasing and reaches a maximum value

of 0.00414 K<sup>-1</sup> at 561 K for green emissions and 0.00278 K<sup>-1</sup> at 98 K for red emissions. As a comparison, the optical temperature measurement parameters of several typical materials based on the two thermal coupled states of Er<sup>3+</sup> ions are listed in Table 1. From Fig. 5c, these two  $S_a$  curves cross at about 240 K, indicating that green thermometry is appropriate for high temperatures (>240 K) and red thermometry is suitable for low temperatures (<240 K). Hence, dual-color thermometry shows a wide temperature sensing range of which the  $S_a$  is always maintained at high values. In contrast, c-ZrO<sub>2</sub> could only implement the red scheme because the green UCL could almost be ignored. The cycling experiment has been carried out and the FIR at specific temperature is plotted in Fig. 5e and Fig. S2 (ESI<sup>†</sup>). The data points only show small deviations from the average values (dashed lines) for both green and red schemes, indicating the high durability and reproducibility of m-ZrO<sub>2</sub> for optical thermometry. Besides, m-ZrO<sub>2</sub> shows a comparable sensitivity relative to other binary oxides.<sup>37-41</sup> Based on eqn (1)-(3),  $S_r$  and the temperature ( $T_{\text{max}}$ ) at which  $S_a$  reaches the maximum are both determined by  $\Delta E$ . Accordingly,

Table 1 Optical thermometry parameters of some materials based on two thermally coupled states of Er<sup>3+</sup>

Sensing materials	Temperature range (K)	$\Delta E$ (cm <sup>-1</sup> )	$S_a \times 10^{-3}$ (K <sup>-1</sup> )	Ref.
m-ZrO <sub>2</sub> :Yb <sup>3+</sup> ,Er <sup>3+</sup>	83–563	780	4.1 (561 K)	This work
LaGdO <sub>3</sub> :Er <sup>3+</sup>	298–873	737	4.3 (554 K)	33
Ba <sub>3</sub> Y <sub>4</sub> O <sub>9</sub> :Yb <sup>3+</sup> ,Er <sup>3+</sup>	83–563	800	2.5 (563 K)	34
Gd <sub>2</sub> O <sub>3</sub> :Yb <sup>3+</sup> ,Er <sup>3+</sup>	300–900	545	3.9 (554 K)	39
Y <sub>2</sub> O <sub>3</sub> :Yb <sup>3+</sup> ,Er <sup>3+</sup>	93–613	615.7	4.4 (427 K)	40
La <sub>2</sub> O <sub>3</sub> :Yb <sup>3+</sup> ,Er <sup>3+</sup>	313–573	822.4	6.6 (573 K)	41

changing the host is necessary to achieve different energy gaps for various temperature sensing applications using the  $\text{Er}^{3+}\text{-Yb}^{3+}$  UC system.

The temperature resolution of 0.031–0.36 K in the range of 83 to 563 K is estimated using eqn (S1) and (S2) (ESI<sup>†</sup>),<sup>42</sup> indicating that the optical thermometer has high precision in temperature sensing.

## 4. Conclusion

We have successfully prepared  $\text{Er}^{3+}$  and  $\text{Yb}^{3+}$  heavily codoped m- $\text{ZrO}_2$  by incorporating  $\text{Nb}^{5+}$  as charge compensation. The UC integrated intensity of the m- $\text{ZrO}_2$  is 4-fold higher than that of c- $\text{ZrO}_2$  with their optimal concentrations. The comparative study reveals that the m- $\text{ZrO}_2$  has faster radiative transition rates of  $\text{Er}^{3+}$  and  $\text{Yb}^{3+}$  than those of the c- $\text{ZrO}_2$ . The enhanced radiative transition allows a lower  $\text{Yb}^{3+}$  optimal concentration, thus retaining lower energy back transfer from  $\text{Er}^{3+}$  in the green emitting state to  $\text{Yb}^{3+}$  and lower concentration quenching of  $\text{Yb}^{3+}$  in the monoclinic phase. Therefore, m- $\text{ZrO}_2$  shows both strong green and red UC emissions, while the red emission dominates the luminescence in c- $\text{ZrO}_2$ . The optical thermometry measurements exhibit that the maximum absolute sensitivities are 0.00414 and 0.00278  $\text{K}^{-1}$  for green and red schemes, respectively. The green and red thermometers are complementary schemes that green thermometry is appropriate for high temperatures (>240 K) and red thermometry is suitable for low temperatures (<240 K). These results suggest that  $\text{Er}^{3+}/\text{Yb}^{3+}$  heavily doped m- $\text{ZrO}_2$  is a promising candidate for efficient UCL and dual-color thermometry.

## Conflicts of interest

The authors declare no competing financial interest.

## Acknowledgements

This work was supported by the National Natural Science Foundation of China (Grant No. 11904361, 12074374, 11874055, 11974346, 51772286), Youth Innovation Promotion Association CAS No. 2020222, Cooperation project between Jilin Province and the Chinese Academy of Sciences (2020SYHZ0013).

## References

- R. R. Deng, F. Qin, R. F. Chen, W. Huang, M. H. Hong and X. G. Liu, Temporal full-colour tuning through non-steady-state upconversion, *Nat. Nanotechnol.*, 2015, **10**, 237–242.
- F. Wang, S. H. Wen, H. He, B. M. Wang, Z. G. Zhou, O. Shimoni and D. Y. Jin, Microscopic inspection and tracking of single upconversion nanoparticles in living cells, *Light: Sci. Appl.*, 2018, **7**, e18007.
- C. Zhang, L. Yang, J. Zhao, B. H. Liu, M. Y. Han and Z. P. Zhang, White-Light Emission from an Integrated Upconversion Nanostructure: Toward Multicolor Displays Modulated by Laser Power, *Angew. Chem., Int. Ed.*, 2015, **54**, 11531–11535.
- K. C. Liu, Z. Y. Zhang, C. X. Shan, Z. Q. Feng, J. S. Li, C. L. Song, Y. N. Bao, X. H. Qi and B. Dong, A flexible and superhydrophobic upconversion-luminescence membrane as an ultrasensitive fluorescence sensor for single droplet detection, *Light: Sci. Appl.*, 2016, **5**, e16136.
- X. Chen, L. M. Jin, W. Kong, T. Y. Sun, W. F. Zhang, X. H. Liu, J. Fan, S. F. Yu and F. Wang, Confining energy migration in upconversion nanoparticles towards deep ultraviolet lasing, *Nat. Commun.*, 2016, **7**, 10304.
- S. Fischer, E. Favilla, M. Tonelli and J. C. Goldschmidt, Record efficient upconverter solar cell devices with optimized bifacial silicon solar cells and monocrystalline  $\text{BaY}_2\text{F}_8:30\%\text{Er}^{3+}$  upconverter, *Sol. Energy Mater. Sol. Cells*, 2015, **136**, 127–134.
- J. H. Zhang, Z. D. Hao, J. Li, X. Zhang, Y. S. Luo and G. H. Pan, Observation of efficient population of the red-emitting state from the green state by non-multiphonon relaxation in the  $\text{Er}^{3+}\text{-Yb}^{3+}$  system, *Light: Sci. Appl.*, 2015, **4**, e239.
- H. X. Mai, Y. W. Zhang, L. D. Sun and C. H. Yan, Highly efficient multicolor up-conversion emissions and their mechanisms of monodisperse  $\text{NaYF}_4:\text{Yb},\text{Er}$  core and core/shell-structured nanocrystals., *J. Phys. Chem. C*, 2007, **111**, 13721–13729.
- R. G. Geitenbeek, P. T. Prins, W. Albrecht, A. van Blaaderen, B. M. Weckhuysen and A. Meijerink,  $\text{NaYF}_4:\text{Er}^{3+},\text{Yb}^{3+}/\text{SiO}_2$  Core/Shell Upconverting Nanocrystals for Luminescence Thermometry up to 900 K, *J. Phys. Chem. C*, 2017, **121**, 3503–3510.
- A. Patra, C. S. Friend, R. Kapoor and P. N. Prasad, Effect of crystal nature on upconversion luminescence in  $\text{Er}^{3+}:\text{ZrO}_2$  nanocrystals, *Appl. Phys. Lett.*, 2003, **83**, 284.
- L. Liu, Y. X. Wang, X. R. Zhang, K. Yang, Y. F. Bai, C. H. Huang and Y. L. Song, Optical thermometry through green and red upconversion emissions in  $\text{Er}^{3+}/\text{Yb}^{3+}/\text{Li}^+:\text{ZrO}_2$  nanocrystals, *Opt. Commun.*, 2011, **284**, 1876–1879.
- J. Zhou, C. Li, R. S. Lei, H. P. Wang, M. H. Li, D. H. Li, Q. H. Yang, Y. J. Hua and S. Q. Xu, Novel Optical Thermometry Strategy Based on  $\text{Gd}_3$  and Defect-Related Luminescence of  $\text{ZrO}_2:\text{Gd}^{3+}$  Nanoparticles, *J. Phys. Chem. C*, 2020, **124**, 21664–21673.
- H. S. Loksha, K. R. Nagabhushana, M. L. Chithambo and F. Singh, Down and upconversion photoluminescence of  $\text{ZrO}_2:\text{Er}^{3+}$  phosphor irradiated with 120 MeV gold ions, *Mater. Res. Express*, 2020, **7**, 064006.
- M. Fois, T. Cox, N. Ratcliffe and B. L. Costello, Rare Earth Doped Metal Oxide Sensor for the Multimodal Detection of Volatile Organic Compounds (VOCs), *Sens. Actuators, B*, 2021, **330**, 129264.
- M. Eibl, S. Shaw, D. Prieur, A. Rossberg, M. C. Wilding, C. Henning, K. Morris, J. Rothe, T. Stumpf and N. Huitinen, Understanding the local structure of Eu- and Y-stabilized zirconia: insights from luminescence and X-ray absorption spectroscopic investigations, *J. Mater. Sci.*, 2020, **55**, 10095–10120.
- G. H. Pan, L. L. Zhang, H. J. Wu, X. S. Qu, H. Wu, Z. Hao, L. Zhang, X. Zhang and J. H. Zhang, On the luminescence of  $\text{Ti}^{4+}$  and  $\text{Eu}^{3+}$  in monoclinic  $\text{ZrO}_2$ : high performance optical thermometry derived from energy transfer, *J. Mater. Chem. C*, 2020, **8**, 4518–4533.



- 17 J. H. Hao, Y. Zhang and X. H. Wei, Electric-induced enhancement and modulation of upconversion photoluminescence in epitaxial BaTiO<sub>3</sub>:Yb/Er thin films, *Angew. Chem., Int. Ed.*, 2011, **50**, 6876–6880.
- 18 M. Wisser, M. Chea, Y. Lin, D. Wu, W. Mao, A. Salleo and J. Dionne, Strain-Induced Modification of Optical Selection Rules in Lanthanide-Based Upconverting Nanoparticles, *Nano Lett.*, 2015, **15**, 1891–1897.
- 19 D. Avram, C. Colbea and C. Tiseanu, Effects of local symmetry on upconversion emission mechanisms under pulsed excitation, *J. Mater. Chem. C*, 2019, **7**, 13770–13777.
- 20 L. Liu, Y. J. Chen, X. L. Zhang, Y. X. Wang, X. R. Zhang and Y. L. Song, Enhanced upconversion fluorescence of Er<sup>3+</sup>:ZrO<sub>2</sub> nanocrystals induced by phase transformation, *AIP Adv.*, 2012, **2**, 012102.
- 21 P. Li, I. W. Chen and J. E. Penner-Hahn, Effect of Dopants on Zirconia Stabilization—An X-ray Absorption Study: I, Trivalent Dopants, *J. Am. Ceram. Soc.*, 1994, **77**, 118–128.
- 22 P. Li, I. W. Chen and J. E. Penner-Hahn, Effect of Dopants on Zirconia Stabilization—An X-ray Absorption Study: III, Charge-Compensating Dopants, *J. Am. Ceram. Soc.*, 1994, **77**, 1289–1295.
- 23 X. Yin, Y. M. Wang, D. Y. Wan, F. Q. Huang and J. Y. Yao, Red-luminescence enhancement of ZrO<sub>2</sub>-based phosphor by codoping Eu<sup>3+</sup> and M<sup>3+</sup> (M = Nb, Ta), *Opt. Mater.*, 2012, **34**, 1353–1356.
- 24 A. Wiatrowska and E. Zych, Modeling Luminescent Properties of HfO<sub>2</sub>:Eu Powders with Li, Ta, Nb, and V Codopants, *J. Phys. Chem. C*, 2012, **116**, 6409–6419.
- 25 K. Smits, A. Sarakovskis, L. Grigorjeva, D. Millers and J. Grabis, The role of Nb in intensity increase of Er ion upconversion luminescence in zirconia, *J. Appl. Phys.*, 2014, **115**, 213520.
- 26 D. Y. Lee, J. W. Jang and D. J. Kim, Raman spectral characterization of existing phases in the ZrO<sub>2</sub>-Y<sub>2</sub>O<sub>3</sub>-Nb<sub>2</sub>O<sub>5</sub> system., *Ceram. Inter.*, 2001, **27**, 291–298.
- 27 C. G. Kontoyannis and M. Orkoulou, Quantitative determination of the cubic, tetragonal and monoclinic phases in partially stabilized zirconias by Raman spectroscopy, *J. Mater. Sci.*, 1994, **29**, 5316–5320.
- 28 R. H. French, S. J. Glass, F. S. Ohuchi, Y.-N. Xu and W. Y. Ching, Experimental and theoretical determination of the electronic structure and optical properties of three phases of ZrO<sub>2</sub>, *Phys. Rev. B: Condens. Matter Mater. Phys.*, 1994, **49**, 5133–5142.
- 29 F. Gallino, C. D. Valentin and G. Pacchioni, Band gap engineering of bulk ZrO<sub>2</sub> by Ti doping, *Phys. Chem. Chem. Phys.*, 2011, **13**, 17667–17675.
- 30 M. Pollnau, D. R. Gamelin, S. R. Lüthi and H. U. Güdel, Power dependence of upconversion luminescence in lanthanide and transition-metal-ion systems, *Phys. Rev. B: Condens. Matter Mater. Phys.*, 2000, **61**, 3337.
- 31 J. T. Kong, X. Y. Shang, W. Zhang, X. Y. Chen, D. T. Tu, M. Wang, J. Song and J. L. Qu, Revisiting the Luminescence Decay Kinetics of Energy Transfer Upconversion, *J. Phys. Chem. Lett.*, 2020, **11**, 3627–3680.
- 32 Y. Li, W. M. Wang, Y. Pan, H. M. Chen, Q. W. Cao and X. T. Wei, Upconversion luminescence and optical thermometry properties of transparent oxyfluoride glass ceramics embedded with Ba<sub>4</sub>Y<sub>3</sub>F<sub>17</sub>: Yb<sup>3+</sup>, Er<sup>3+</sup> nanocrystals, *CrystEngComm*, 2020, **22**, 6302–6309.
- 33 V. Gutiérrez-Cano, F. Rodríguez, J. A. González and R. Valiente, Valiente, Upconversion and Optical Nanothermometry in LaGdO<sub>3</sub>: Er<sup>3+</sup> Nanocrystals in the RT-900 K Range, *J. Phys. Chem. C*, 2019, **123**, 29818–29828.
- 34 H. Wu, Z. D. Hao, L. L. Zhang, X. Zhang, Y. Xiao, G. H. Pan, H. J. Wu, Y. S. Luo, L. G. Zhang and J. H. Zhang, Er<sup>3+</sup>/Yb<sup>3+</sup> codoped phosphor Ba<sub>3</sub>Y<sub>4</sub>O<sub>9</sub> with intense red upconversion emission and optical temperature sensing behaviour, *J. Mater. Chem. C*, 2018, **6**, 3459–3467.
- 35 S. A. Wade, S. F. Collins and G. W. Baxter, Fluorescence intensity ratio technique for optical fiber point temperature sensing, *J. Appl. Phys.*, 2003, **94**, 4743–4756.
- 36 D. X. Chen, L. L. Zhang, Y. J. Liang, W. L. Wang, S. Yan, J. Q. Bi and K. N. Sun, Yolk-shell structured Bi<sub>2</sub>SiO<sub>5</sub>:Yb<sup>3+</sup>, Ln<sup>3+</sup> (Ln = Er, Ho, Tm) upconversion nanophosphors for optical thermometry and solid-state lighting, *CrystEngComm*, 2020, **22**, 4438–4448.
- 37 X. Wang, X. G. Kong, Y. Yu, Y. J. Sun and H. Zhang, Effect of Annealing on Upconversion Luminescence of ZnO: Er<sup>3+</sup> Nanocrystals and High Thermal Sensitivity, *J. Phys. Chem. C*, 2007, **111**, 15119–15124.
- 38 B. S. Cao, Y. Y. He, Y. Sun, M. Song and B. Dong, Optical high temperature sensor based on enhanced green upconversion emissions in Er<sup>3+</sup>-Yb<sup>3+</sup>-Li<sup>+</sup> codoped TiO<sub>2</sub> powders, *J. Nanosci. Nanotechnol.*, 2011, **11**, 9899–9903.
- 39 S. K. Singh, K. Kumar and S. B. Rai, Er<sup>3+</sup>/Yb<sup>3+</sup> codoped Gd<sub>2</sub>O<sub>3</sub> nano-phosphor for optical thermometry, *Sens. Actuators, A*, 2009, **149**, 16–20.
- 40 P. Du, L. H. Luo, Q. Y. Yue and W. P. Li, The simultaneous realization of high- and low-temperature thermometry in Er<sup>3+</sup>/Yb<sup>3+</sup>-codoped Y<sub>2</sub>O<sub>3</sub> nanoparticles, *Mater. Lett.*, 2015, **143**, 209–211.
- 41 Z. Sun, G. F. Liu, Z. L. Fu, T. Q. Sheng, Y. L. Wei and Z. J. Wu, Nanostructured La<sub>2</sub>O<sub>3</sub>: Yb<sup>3+</sup>/Er<sup>3+</sup>: Temperature sensing, optical heating and bio-imaging application, *Mater. Res. Bull.*, 2017, **92**, 39–45.
- 42 Q. Wang, M. Liao, Z. F. Mu, X. Zhang, H. F. Dong, Z. J. Liang, J. C. Luo, Y. Yang and F. G. Wu, Ratiometric Optical Thermometer with High Sensitivity Based on Site-Selective Occupancy of Mn<sup>2+</sup> Ions in Li<sub>5</sub>Zn<sub>8</sub>Al<sub>5</sub>Ge<sub>9</sub>O<sub>36</sub> under Controllable Synthesis Atmosphere, *J. Phys. Chem. C*, 2020, **124**, 886–895.